

MIT Open Access Articles

Poor Stability of Li_2CO_3 in the Solid Electrolyte Interphase of a Lithium#Metal Anode Revealed by Cryo#Electron Microscopy

The MIT Faculty has made this article openly available. **Please share** how this access benefits you. Your story matters.

Citation: Han, Bing, Zhang, Zhen, Zou, Yucheng, Xu, Kang, Xu, Guiyin et al. 2021. "Poor Stability of Li_2CO_3 in the Solid Electrolyte Interphase of a Lithium#Metal Anode Revealed by Cryo#Electron Microscopy." *Advanced Materials*, 33 (22).

As Published: <http://dx.doi.org/10.1002/adma.202100404>

Publisher: Wiley

Persistent URL: <https://hdl.handle.net/1721.1/140338>

Version: Author's final manuscript: final author's manuscript post peer review, without publisher's formatting or copy editing

Terms of use: Creative Commons Attribution-Noncommercial-Share Alike



Poor Stability of Li_2CO_3 in Solid Electrolyte Interphase of Li Metal Anode Revealed by Cryo-Electron Microscopy

Bing Han^{†,1,2}, Zhen Zhang^{†,1}, Yucheng Zou¹, Kang Xu³, Guiyin Xu⁴, Hong Wang¹, Hong Meng²,
Yonghong Deng^{1,*}, Ju Li^{4,*}, Meng Gu^{1,*}

¹Department of Materials Science and Engineering, and Guangdong Provincial Key Laboratory of Energy Materials for Electric Power, Southern University of Science and Technology, Shenzhen 518055, China

²Advanced Materials, Peking University Shenzhen Graduate School, Shenzhen, 518055 China

³Energy Storage Branch, Sensors and Electron Devices Directorate, US Army Research Laboratory, 2800 Powder Mill Rd., Adelphi, Maryland 20783, USA

⁴Department of Nuclear Science and Engineering and Department of Materials Science and Engineering, Massachusetts Institute of Technology, Cambridge, MA 02139, USA

[†]These authors contributed equally to this work.

*Correspondence to: yhdeng08@163.com (Y. Deng); gum@sustech.edu.cn (M. Gu);
liju@mit.edu (J. Li)

Abstract: Solid electrolyte interphase (SEI) dictates the cycling stability of lithium metal batteries. Here, we achieve direct atomic imaging of the SEI's phase components and their spatial arrangement, using ultra low-dosage cryo-TEM. Our results showed that surprisingly, a lot of the deposited Li metal has amorphous atomic structure, likely due to carbon and oxygen impurities, and that crystalline lithium carbonate is not stable and readily decomposes when contacting the lithium metal. Lithium carbonate distributed in the outer SEI also continuously reacts with the electrolyte to produce gas, resulting in a dynamically evolving and porous SEI. Sulfur-containing additives cause the SEI to preferentially generate overlithiated lithium sulfate and lithium oxide, which

This is the author manuscript accepted for publication and has undergone full peer review but has not been through the copyediting, typesetting, pagination and proofreading process, which may lead to differences between this version and the [Version of Record](#). Please cite this article as [doi: 10.1002/adma.102100404](#).

This article is protected by copyright. All rights reserved.

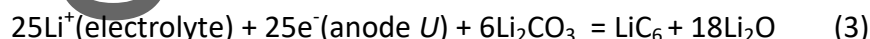
encapsulates lithium carbonate in the middle, limiting further SEI thickening and enhancing battery life by a factor of ten. Our spatial mapping of the SEI gradient amorphous (polymeric→inorganic→metallic) and crystalline phase components provides guidance for designing electrolyte additives.

Main Text:

Lithium metal in the body-centered cubic phase (Li_{BCC}) has long been regarded as the ultimate anode for rechargeable batteries, due to its high specific capacity (3860 mAh g^{-1}) and low redox potential (-3.040 V versus standard hydrogen electrode)¹⁻⁹. The structural, chemical, electronic, and mechanical properties of the solid electrolyte interphase (SEI) play a critical role in determining the stability of the anode¹⁰⁻¹². The SEI is supposed to be a self-passivating layer that forms as the battery cycles, coating the anode and electronically insulating the electrolyte from the free electrons in the anode while remaining conductive to Li^+ cations^{13, 14}. Polyanion compounds such as lithium carbonate Li_2CO_3 and lithium sulfate Li_2SO_4 are long thought to be SEI components that directly contact Li_{BCC} , playing the role of the electronic insulator^{15, 16}. However, thermodynamically, the following reactions



have large driving forces for the decomposition of the polyanions toward the right-hand side (see Table S1). Indeed, none of the well-known polyanion compounds, nitrate NO_3^- , phosphate PO_4^{3-} , silicate SiO_4^{4-} , etc. appear to be thermodynamically stable in contact with Li_{BCC} , either. And when considering half-cell reaction like



as the computed equilibrium voltage is around $+1 \text{ V}$ versus Li_{BCC} , one has to conclude that Li_2CO_3 and Li_2SO_4 should not be stable in direct contact with the graphite anode in conventional lithium-ion batteries either¹⁷, wherever free electrons can tunnel to from the said anodes, as $\text{Li}^+(\text{electrolyte})$ must be available there by the definition of SEI¹⁸. This means the SEI, if it contains lithium polyanion compounds, must be a nanocomposite with stable buffer phases near the Li metal. Because Li_2O and Li_2S are wide band-gap insulators, they are the more likely the “innermost” SEI components that electronically insulate the

polyanionic compounds, if they indeed exist. However, one of the decomposition products in (1) and (3), LiC_6 , or more broadly LiC_x ($x=6,12$, or other forms of lithiated carbon), are not electronically insulating, and will likely facilitate electron tunneling by tip-enhanced electron emission due to the extremely small radii of curvature of such metallic phases. So one naturally suspects that lithium carbonate Li_2CO_3 will not be a very stable SEI component, at least on the inside, compared to Li_2SO_4 , since the right-hand side of (1) could be electronically more conductive than the right-hand side of (2). This is perhaps the reason that organic carbonate liquid electrolytes need to be supplemented by fluorine- and sulfur-containing additives, to stop the SEI from thickening indefinitely due to LiC_x . Also, it is known that the SEI on the anode surface is extremely sensitive to air and moisture, and undergoes a dynamic formation and rupture-repair process with the constant consumption of electrolyte and lithium ions during battery cycling. An intrinsically unstable SEI results in electrolyte depletion and rapid "death" of a battery^{19, 20}. For all the reasons above, we need clear atomic-scale imaging of the SEI.

Although techniques such as X-ray Photoemission Spectroscopy (XPS)^{21, 22} can readily determine the rough chemical composition of the SEI, it lacks the spatial resolution and diffraction capability to accurately distinguish phase structures at the nano- or atomic scale to draw accurate mechanistic conclusions with regard to electrolyte additives. Indeed, by mere chemical analyses, one would find it difficult to distinguish between Li_2CO_3 and "overlithiated Li_2CO_3 ", defined to be the mixture of the right-hand side of (1) plus retained Li_2CO_3 phase. Conventional TEM can easily damage the SEI due to its vulnerability to the electron beam, moisture, and oxygen during the TEM sample preparation and sample transfer. Recently, atomic-scale characterization of SEI using cryogenic TEM (cryo-TEM) can identify the chemical phases and locations of the randomly distributed inorganic and organic ingredients at the atomic scale²³⁻²⁷. In this work, we pushed the cryo-TEM to its resolution limit with ultra-low electron-beam dosage and successfully imaged the native SEI on Li metal electrode at the atomic scale. We also conduct cryo-electron energy loss spectroscopy (cryo-EELS) mapping, giving us a comprehensive picture of the SEI's chemistry, and vital information about the influence of the electrolyte additive on the lithium metal morphology²⁸⁻³¹. With such high-resolution cryo-TEM (HRTEM) analysis, we reveal a clear gradient distribution of phases, including three types of amorphous phases: an outermost organic polymeric amorphous phase $\text{Polymer}_{\text{Amor}}$, an amorphous oxide-sulfide phase in the

middle $\text{Inorg}_{\text{Amor}}$, and a metallic Li_{Amor} phase in the interior, with increasing electronic conductivity as one goes from the liquid electrolyte side to the Li_{BCC} side. Crystalline phases of Li_2CO_3 , Li_2SO_4 , Li_2O are dispersed within these amorphous phases. In this paper, we compare the SEI structure grown using three electrolytes- commercial pure carbonates EC-DEC (Ethylene Carbonate $(\text{CH}_2\text{O})_2\text{CO}$ - Diethyl Carbonate $(\text{CH}_3\text{CH}_2\text{O})_2\text{CO}$) electrolyte without any additive, with 2% DTD (Ethylene Sulfate $\text{C}_2\text{H}_4\text{O}_4\text{S}$), or with 2% PS (1,3-propanesulfonate $\text{C}_3\text{H}_6\text{O}_3\text{S}$), respectively, revealing the poor stability of Li_2CO_3 and additives' influence on the SEI formation. It appears that sulfur-containing electrolytes show superior performance because the "overlithiated Li_2SO_4 ", $\text{Li}_2\text{S}+4\text{Li}_2\text{O}$, on the inside, are much more electronically insulating. Also, Li_2SO_4 formed on the exterior of SEI appear to be much more stable than Li_2CO_3 , and protect the crystalline Li_2CO_3 sandwiched in the middle.

Microstructures of Li_{Metal} and SEI

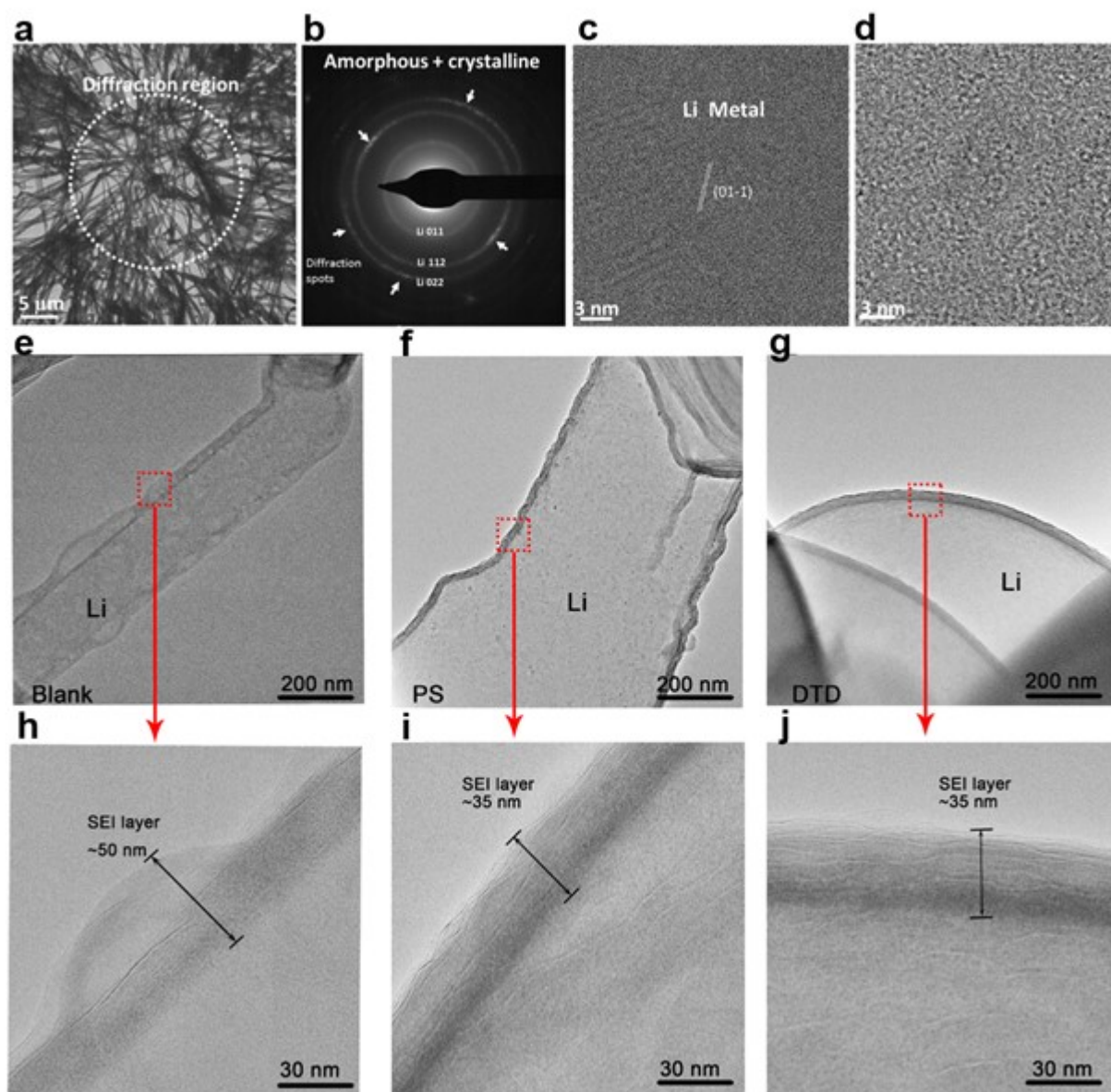


Fig. 1. **a**, overall cryo-TEM view of the Li dendrites morphology deposited in the commercial EC-based electrolytes. **b**, electron diffraction pattern of the region labeled in white in panel (**a**). **c**, representative cryo-HRTEM image of the crystalline Li dendrite region. **d**, representative cryo-HRTEM image of the disordered amorphous Li dendrite region. **e, h**, cryo-TEM images of lithium dendrites deposited and enlarged view of the selected SEI part in the commercial EC-based electrolytes. **f, i**, the same in the PS-containing electrolytes. and **g, h**, the same in the DTD-containing electrolytes. Images are obtained at an electron dosage $\sim 100 \text{ e}/\text{\AA}^2$

In the coarse-scale cryo-TEM images in Fig. 1a, the as-formed lithium dendrites are quite long (up to tens of micrometers), with diameters ranging from 100 nm to about 500

nm and atomic structures that can be either amorphous or crystalline. The selected area electron diffraction in Fig. 1b shows the signature of bands of amorphous Li dendrites punctuated by crystalline Li_{BCC} diffraction spots, as marked by the white arrows. Therefore, the as-grown Li dendrites contain a portion of disordered amorphous Li metal phase, denoted as Li_{Amor} . Wang et al reported that the glassy Li metal formation is kinetically driven and related to the battery current density and deposition time³². The high-resolution cryo-TEM image in Fig. 1c shows a representative crystalline dendrite region with $(01\bar{1})_{\text{LiBCC}}$ lattice planes. In contrast, Fig. 1d shows a representative amorphous dendrite region, with little crystalline islands (3-5 nm) distributed inside, which can be indexed to small Li_{BCC} or Li_2O crystals. High-resolution TEM (HRTEM) analysis is consistent with the overall electron diffraction analysis, proving that both crystalline Li_{BCC} and amorphous Li_{Amor} are present in the as-grown dendrites. The origin of the amorphous Li metal phase may be attributed to chemical impurities, as monatomic Li metal should crystallize very easily, given that the electrodeposition occurred at 2/3 of Li_{BCC} 's bulk melting point and diffusion is known to be facile at room temperature¹. We speculate that carbon, oxygen on the order of 10 at% contribute to the amorphization of Li metal. These come from the *in operando* decomposition of the liquid electrolyte as $\text{Li}^+(\text{electrolyte}) + \text{e}^-(\text{anode } U) = \text{neutral Li atom}$ is being deposited simultaneously. The crystallinity of our dendrites is seen to vary from region to region, thus such amorphization should depend on a number of factors such as deposition rates and additives. Despite the amorphous nature, Li_{Amor} should still be metallic. From now on, we will use Li_{Metal} to denote multi-phase mixtures of $\text{Li}_{\text{BCC}} + \text{Li}_{\text{Amor}}$, and we speculate that the ratio of Li_{Amor} in Li_{Metal} likely reflects the imperfect barrier properties of the incipient SEI. Note that the SEI must spatially show “metal-insulator transition” as one scan across from the Li_{BCC} side to the liquid electrolyte side, and the kinetics of forming such a gradient structure is of great consequence for liquid-electrolyte-based batteries.

Cryo-TEM enables direct atomic-scale imaging of how the morphology and atomic structures of the Li_{Metal} and the SEI change when the liquid electrolyte used contains different additives. In the presence of common carbonate electrolyte without additives, the lithium dendrite growth is more directional (Fig. 1e) and the SEI layer is thick and porous (Fig. 1e and 1h). However, in the presence of electrolyte with DTD additives, the lithium dendrite growth is more isotropic (Fig. 1g) and the SEI layer is thinner, less porous and more uniform (Fig. 1j). Fig. 1e is a cryo-TEM image of lithium dendrites deposited in a commercial

EC-based electrolyte without additives (EC/DEC =1:1, 1.0 mol L⁻¹ LiPF₆). The SEI shows a porous structure that is possibly caused by the CO₂ gas release³³ during the SEI-formation process. The magnified view in Fig. 1h shows that the SEI layer is quite non-uniform, with an outermost bubble-like amorphous organic layer (up to ~30 nm in thickness) on top of a crystalline layer with dark diffraction contrast. The thickness of the inner, inorganic SEI layer ranges from ~20 nm to ~30 nm. Figs. 1f and 1i are cryo-TEM images of lithium dendrites deposited in the PS-containing electrolyte (EC/DEC+ 2% PS). In addition, Fig. 1i shows that the SEI formed in the modified electrolyte is more uniform (Fig. 1h). Further, the 35 nm thick SEI layer formed in the PS-containing and DTD-containing electrolyte shows only a very thin organic layer Polymer_{Amor} of ~a few nm on top of the dark inorganic layer on the Li_{Metal}. The Li_{Metal} protrusions formed in DTD are round-shaped (Fig. 1g), in sharp contrast with the strip-shaped Li_{Metal} dendrites in PS (Fig. 1f). This clearly demonstrates that DTD additives can inhibit the directional growth of Li_{Metal}. Zachman et al reported the finding of crystalline lithium hydride in the Li dendrite²³. However, we did not observe clear signature of such LiH crystalline phase based on statistical HRTEM analysis of tens of different regions at the Li dendrites in all three samples.

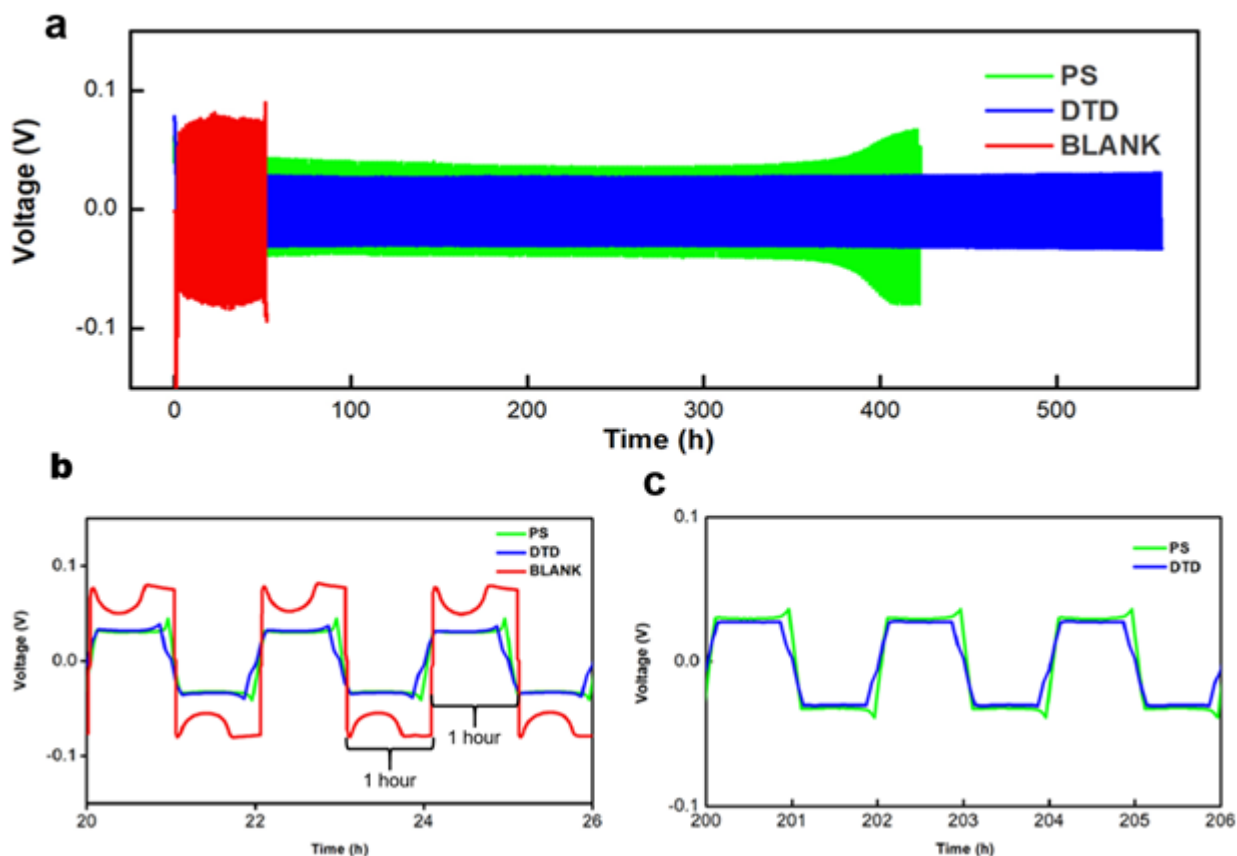


Fig. 2. **a**, Performance of $\text{Li}_{\text{Metal}}|\text{Li}_{\text{Metal}}$ symmetric cells at a current density of $1 \text{ mA}\cdot\text{cm}^{-2}$ using different electrolytes. **b**, voltage profile of symmetric Li-Li cells with DTD/PS/BLANK electrolyte at 20-26 hours. **c**, voltage profile of symmetric Li-Li cells with DTD/PS electrolyte at 200-206 hours.

Because the DTD-containing electrolyte visibly contributes to a more stable solid electrolyte interphase (SEI) and suppression of lithium dendrite growth and gas bubble evolution, we hoped to correlate our structural findings with battery performance. To this end, we assembled and tested symmetric $\text{Li}_{\text{Metal}}|\text{Li}_{\text{Metal}}$ cells with three kinds of electrolytes (DTD/PS/BLANK), as shown in Fig. 2a. The cell with BLANK electrolyte (no additives) deteriorates quickly, even within 20 hours (Figs. 2a and 2b); and the cell impedance diverged and experienced catastrophic failure after 50 hours of cycling. In contrast, the $\text{Li}_{\text{Metal}}|\text{Li}_{\text{Metal}}$ symmetric cell with DTD exhibited highly reversible lithium stripping/plating for over 500 hours. The cycling stability and voltage polarization of the DTD cell even outperformed the PS cell, which retained stability and polarization for 350 hours. It is noteworthy that cell life is the greatest at the lowest polarization, as shown in Fig. 2a to 2c.

Cryo-TEM analysis clearly demonstrates that a stable, uniform, and thin SEI layer corresponds to stable cycling performance of the lithium metal battery. By fitting the impedance with an equivalent circuit in the EIS analysis in Figure S1, the semicircle yields a resistance of the battery is 70 Ω , 150 Ω , 250 Ω in the third cycle of the battery with DTD additive, PS additive, and blank electrolyte, respectively.

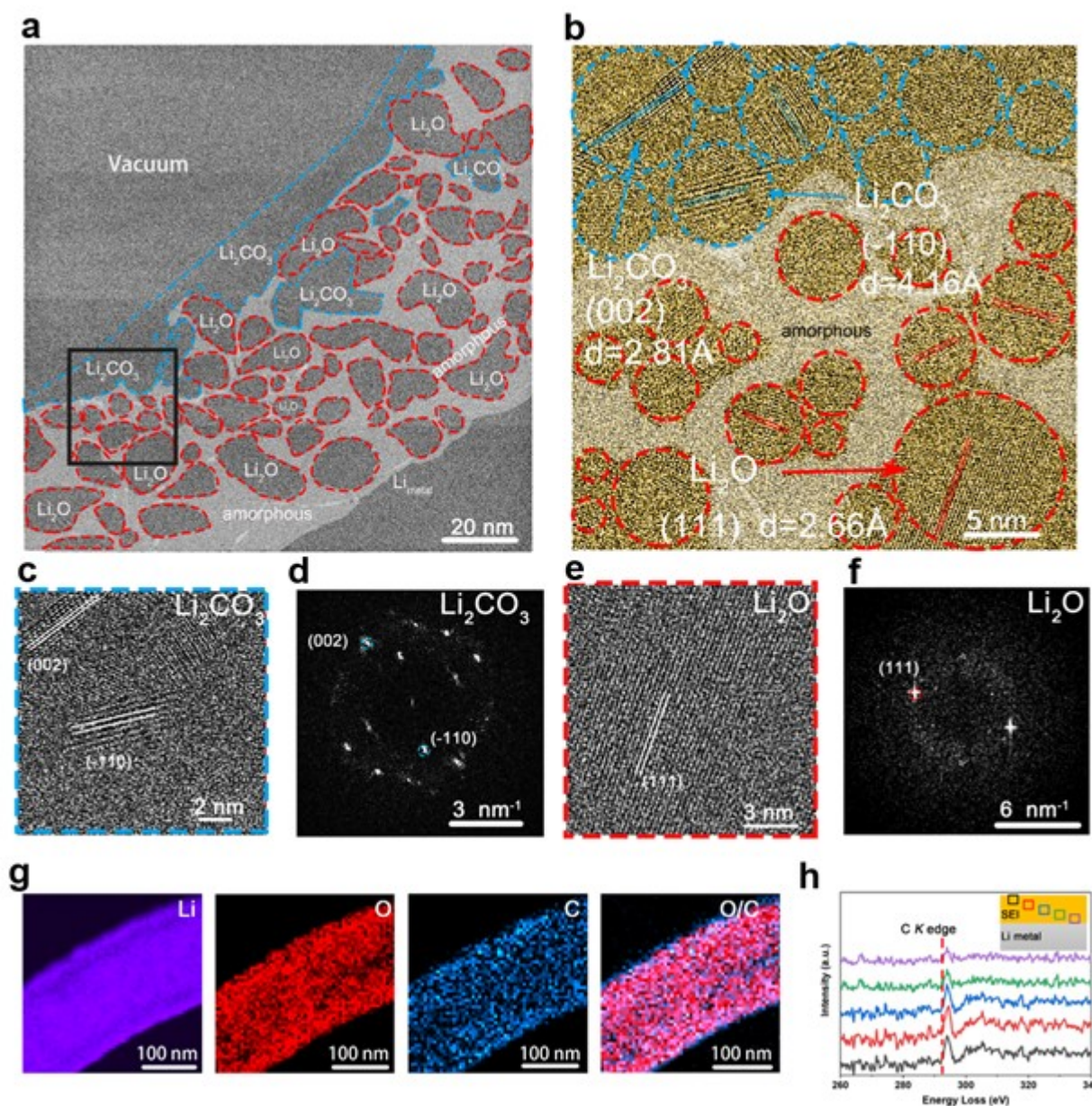


Fig. 3. Cryo-TEM images and elemental compositions of SEI structure in the blank (EC/DEC) Electrolyte acquired using electron dosage $\sim 100\text{e}/\text{\AA}^2$. **a**, phase map of the SEI. **b**, Magnified HRTEM image of black square area in panel A. **c,d**, HRTEM and FFT of Li_2CO_3 crystal. **e,f**, HRTEM and FFT of

Li₂O crystal. **g**, EELS elemental mapping shows the distribution of lithium (purple), oxygen (red) and carbonate (blue) in the lithium dendrites. **h**, The EELS of carbon (C) *K*-edge acquired from Li_{Metal} to SEI surface in (EC/DEC) electrolyte, respectively.

Having shown that the dendrite morphology varies significantly using different electrolytes, we more closely observe the role of the SEI layer in extending the life cycle of Li-metal batteries. To carefully examine the atomic structures of the inorganic layer in the SEI, we performed atomic-resolution cryo-TEM imaging of the SEI in the blank EC/DEC electrolyte (Fig. 3). Fast Fourier transform (FFT) pattern analysis (matching the component's crystal plane spacing to known crystals) reveals that the crystalline parts of SEI contain mainly lithium carbonate and Li₂O (Fig. 3a). Cryo-HRTEM imaging (Fig. 3b) further shows that the top layer of the SEI is comprised of crystalline Li₂CO₃ (blue-dotted region) and the bottom layer is comprised of crystalline Li₂O (red-dotted region), mingling with amorphous regions Polymer_{Amor}+Inorg_{Amor} highlighted in white. The blue-dotted region (Fig. 3c) is lithium carbonate with identifiable ($\bar{1}10$)_{Li₂CO₃}, and (002)_{Li₂CO₃} crystal planes in the corresponding FFT pattern (Fig. 3d). The red-dotted region (Fig. 3e) is comprised of Li₂O with identifiable (111)_{Li₂O} crystal planes (Fig. 3g).

In order to more accurately observe the gradient distribution of Li_{Metal}, crystalline Li₂CO₃, Li₂O, and the spatially percolating Polymer_{Amor}+Inorg_{Amor}, we performed cryo-EELS. From Fig. 3g, we observe that carbon is distributed with higher concentration in the outside layer of the SEI, while oxygen is distributed in all parts of the SEI. Fig. S2 shows the fine structures of the Li, C and O *K*-edge acquired from the center of the dendrite to SEI surface, respectively. The Li *K*-edge spectrum (Fig. S2) of the lithium has a major peak at 60 eV and a minor peak at 65 eV. The outer surface of the SEI has significant O *K*-edge intensity. Meanwhile, the Li *K*-edge spectrum of the surface is weak compared to the Li_{Metal} region. The C *K*-edge spectrum (Fig. 3h) has a major broad peak at 290 eV, implying that the carbon is likely Li₂CO₃. The EELS are consistent with our cryo-TEM imaging and diffraction results, confirming that lithium carbonate is located in the outer part and lithium oxide likely resides at the bottom of the SEI when no additives are added in the electrolyte. Judging from the EELS mapping, the spatially percolating amorphous zones contain Li, O, and possible C elements. The over-lithiated Li₂CO₃ products (Li₂O plus LiC_x) possibly make up the amorphous Inorg_{Amor} in the SEI in direct contact with Li_{Metal}, as highlighted in white in Fig. 3a.

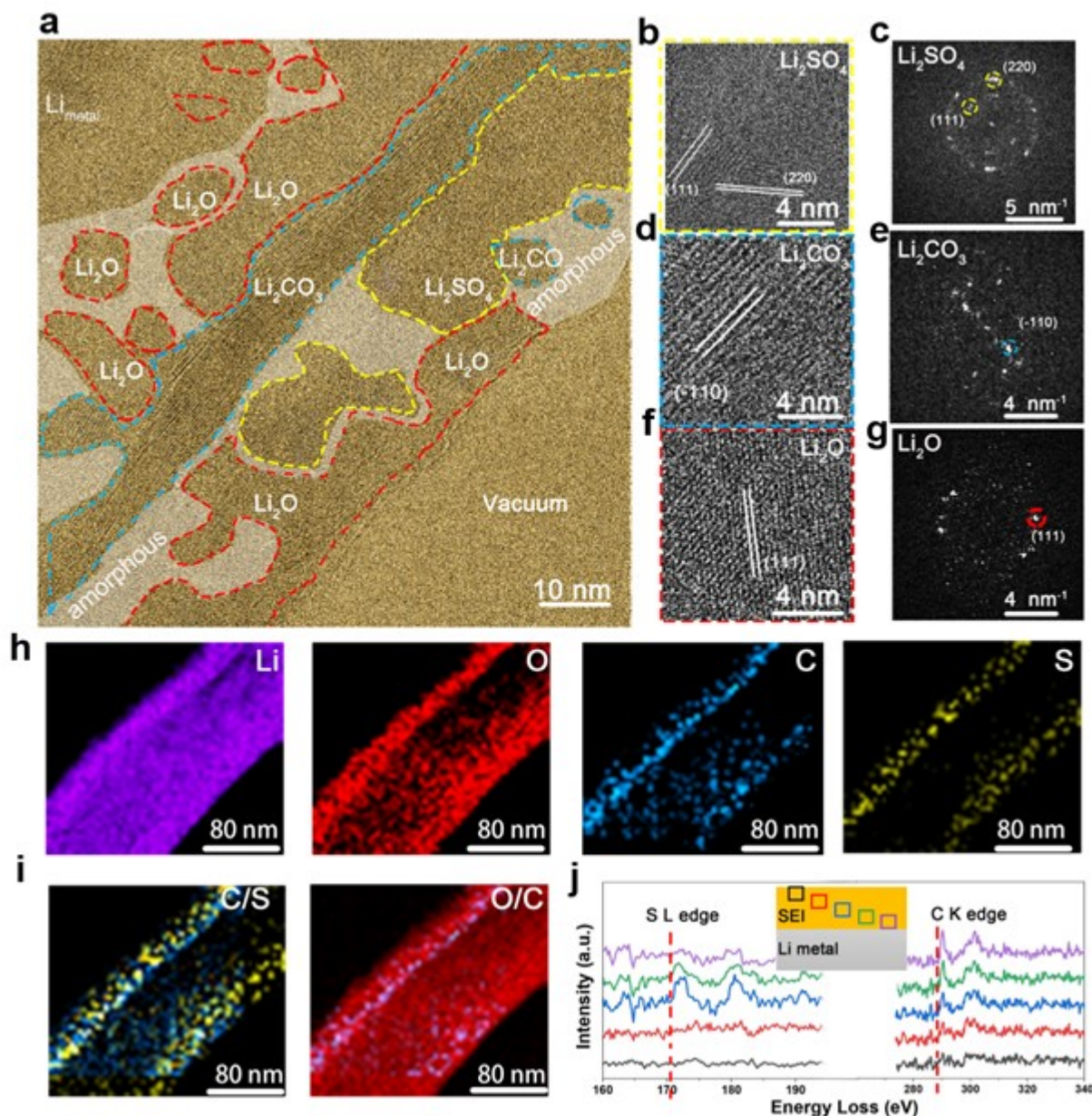


Fig. 4. **a**, Cryo-HRTEM images of SEI in (EC/DEC+ 2%DTD) Electrolyte. **b,c**, HRTEM and FFT of Li_2SO_4 crystal. **d,e**, Li_2CO_3 crystal. **f,g**, Li_2O crystal. **h**, EELS elemental mapping of lithium (purple) in the lithium dendrites. Oxygen (red), carbonate (blue) and sulfur (yellow) in the lithium dendrites. **i**, composite map of carbon and sulfur; oxygen and carbon. **j**, The EELS of S and C K-edge scanning from Li_{Metal} to SEI surface. Please note that the HRTEM images are acquired using the same electron dosage $\sim 100 \text{ e}/\text{\AA}^2$.

The distributions of Li_2O and Li_2CO_3 crystals in SEI vary significantly with additives. The SEI formed in EC/DEC with DTD additive is carefully probed by cryo-TEM and EELS, as

shown in Fig. 4. The lattice-resolution TEM and corresponding FFT analysis proved that the SEI contains Li_2CO_3 , Li_2SO_4 and Li_2O crystals. The cryo-TEM image of SEI depicts that the top layer is mostly Li_2O (red dotted region); the middle layer is predominantly Li_2SO_4 (yellow dotted region) on top of Li_2CO_3 (blue dotted region). Magnified images of the blue dotted region (Fig. 4d) show clearly crystalline grains that are identified to be lithium carbonate with its $(\bar{1}10)_{\text{Li}_2\text{CO}_3}$ crystal planes observed in FFT (Fig. 4e). HRTEM images of the yellow dotted region (Fig. 4b) are large pieces of Li_2SO_4 crystal with observed $(220)_{\text{Li}_2\text{SO}_4}$ and $(111)_{\text{Li}_2\text{SO}_4}$ diffraction spots (Fig. 4c). The (111) crystal planes of Li_2O are identified (Fig. 4f and 4g) as well. Beneath the Li_2CO_3 , there is another layer of Li_2O and inorganic amorphous $\text{Inorg}_{\text{Amor}}$ in contact with the Li_{Metal} , which helps stabilize the whole SEI and provide barrier against electron tunnelling. The $\text{Inorg}_{\text{Amor}}$ zone likely contains the over-lithiated Li_2CO_3 (right-hand side of reaction (1)) and over-lithiated Li_2SO_4 (right-hand side of reaction (2)) products, Li_xO , Li_xS , and LiC_x in amorphous atomic structure, judging from the content identified by EELS. In order to probe the distribution of lithium sulfate, carbonate and oxide at larger scale, we used EELS mapping by tracking the K edges of Li, O, C, and L edge of S at the lithium dendrite with nanoscale resolution in Fig. 4h-4j. Fig. S3 exhibits the fine structures of the Li, C, S and O- K edge acquired from Li_{Metal} to SEI surface, respectively. Similarly, the Li K -edge spectrum in SEI shows oxidized feature, which is consistent with the pronounced O- K edge intensity. The C K -edge spectrum (Fig. 4j) exhibits the Li_2CO_3 signature fine structures. From the C and S peak intensity at different spots, the Li_2SO_4 seems to be distributed more in the top part of the SEI than Li_2CO_3 , which is consistent with HRTEM results. The DTD reacts in the electrolyte and generates Li_2SO_4 , which can cover up some Li_2CO_3 crystalline phases. The Li_2SO_4 layer and Li_2O appear to inhibit the further reaction between lithium carbonate and the electrolyte, resulting in a stable SEI and better cycling stability. Based on statistical HRTEM analysis of a number of locations, we did not locate crystalline Li_2S lattices. However, we detected S L edge from the $\text{Inorg}_{\text{Amor}}$ phase region in the SEI as shown in Figure S5, therefore, we speculate that amorphous Li_xS probably exists in the percolating amorphous regions.

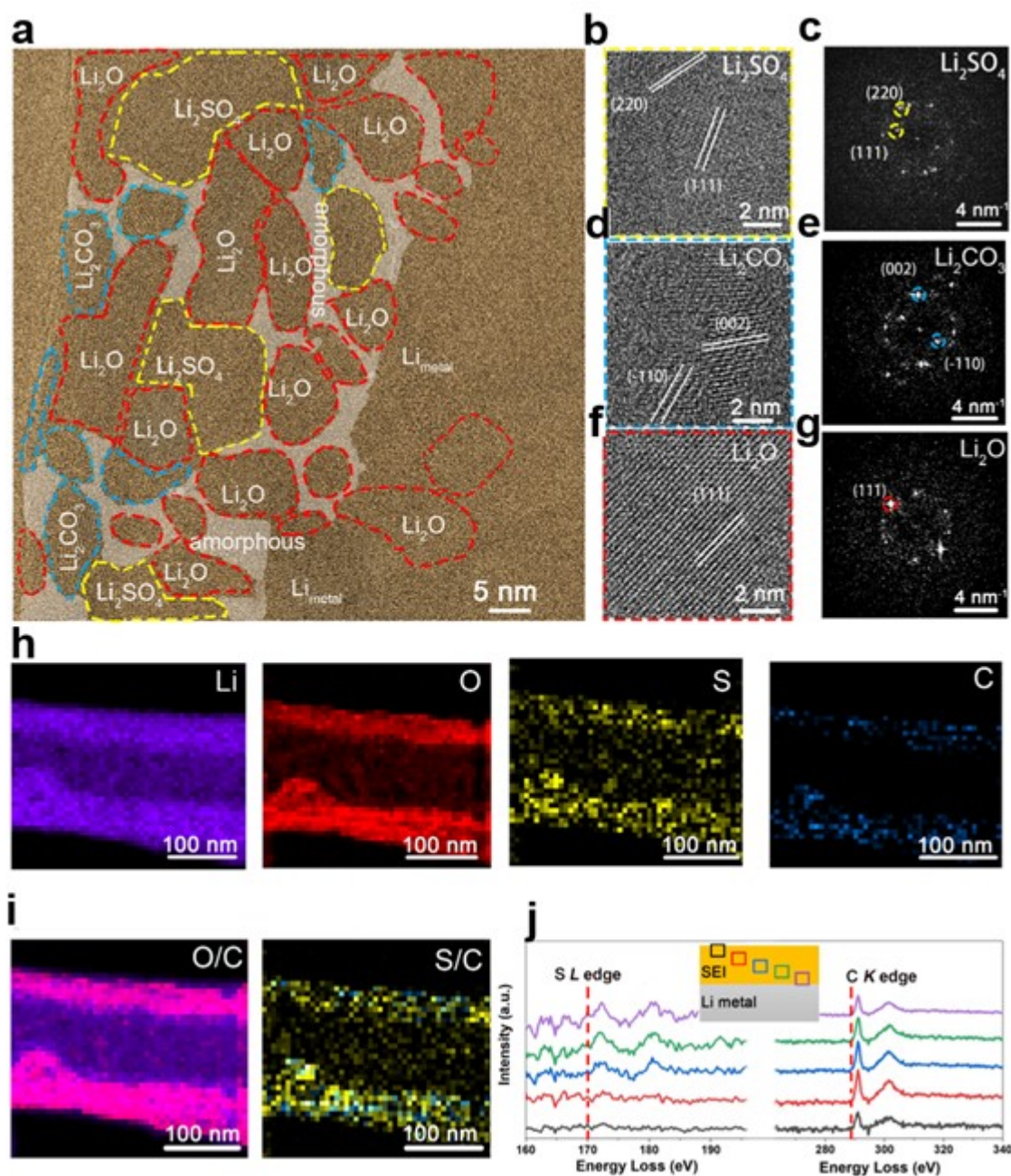


Fig. 5. Cryo-HRTEM images of SEI structure in (EC/DEC+2% PS) Electrolyte. **a**, HRTEM image of the SEI on lithium dendrites acquired using electron dosage $\sim 100\text{e}/\text{\AA}^2$. **b,c**, HRTEM and FFT of Li_2SO_4 crystal. **d,e**, Li_2CO_3 crystal. **f,g**, Li_2O crystal. **h**, EELS elemental mapping shows the distribution of lithium (purple), oxygen (red), sulfur (yellow) and carbonate (blue) in the lithium dendrites. **i**, The combination of carbonate, oxygen and sulfur EELS elemental mapping. **j**, The EELS of S and C K-edge acquired from Li_{Metal} to SEI surface.

In the PS-containing electrolyte, the SEI layer is a mosaic-patterned structure as observed in the cryo-HRTEM micrograph in Fig. 5a. Using FFT analysis in Fig. 5b-g, the SEI contains crystalline Li_2CO_3 , Li_2SO_4 , Li_2O and inorganic amorphous zones. The distribution of lithium oxide and carbonate is less ordered compared to that in the DTD-containing electrolyte. Cryo-HRTEM shows that the top layer contains Li_2CO_3 (blue dotted region) and Li_2O (red dotted region), while the Li_2SO_4 (yellow dotted region) crystals do not completely shield the Li_2CO_3 crystals. There is still a portion of lithium carbonate crystals formed in the outer layer of SEI, inducing gas formation and constantly destabilizing the SEI mechanically. The Li metal region also features a coexistence of both crystalline Li_{BCC} phase and Li_2O phase as circled in red. The EELS mapping displays the distribution of lithium, oxygen, sulfur, and carbon in Fig. 5h. The fine structures of the Li, C, S and O *K*-edge acquired at the SEI are exhibited in Fig. S4, which also indicates the formation of Li_2O , Li_2CO_3 , and Li_2SO_4 . Comparing the S and C signals in Fig. 5j, Li_2SO_4 randomly mixes with the Li_2CO_3 , which is consistent with the cryo-TEM results. The major drawback of PS-containing electrolyte is the existence of a significant portion of naked Li_2CO_3 located in the outer SEI layer, resulting in a worse battery cycling stability than the DTD-containing electrolyte. The highlighted amorphous zones in Fig. 5a containing significant Li, O, and C EELS signals likely result from the decomposition of overlithiated Li_2CO_3 and electrolyte.

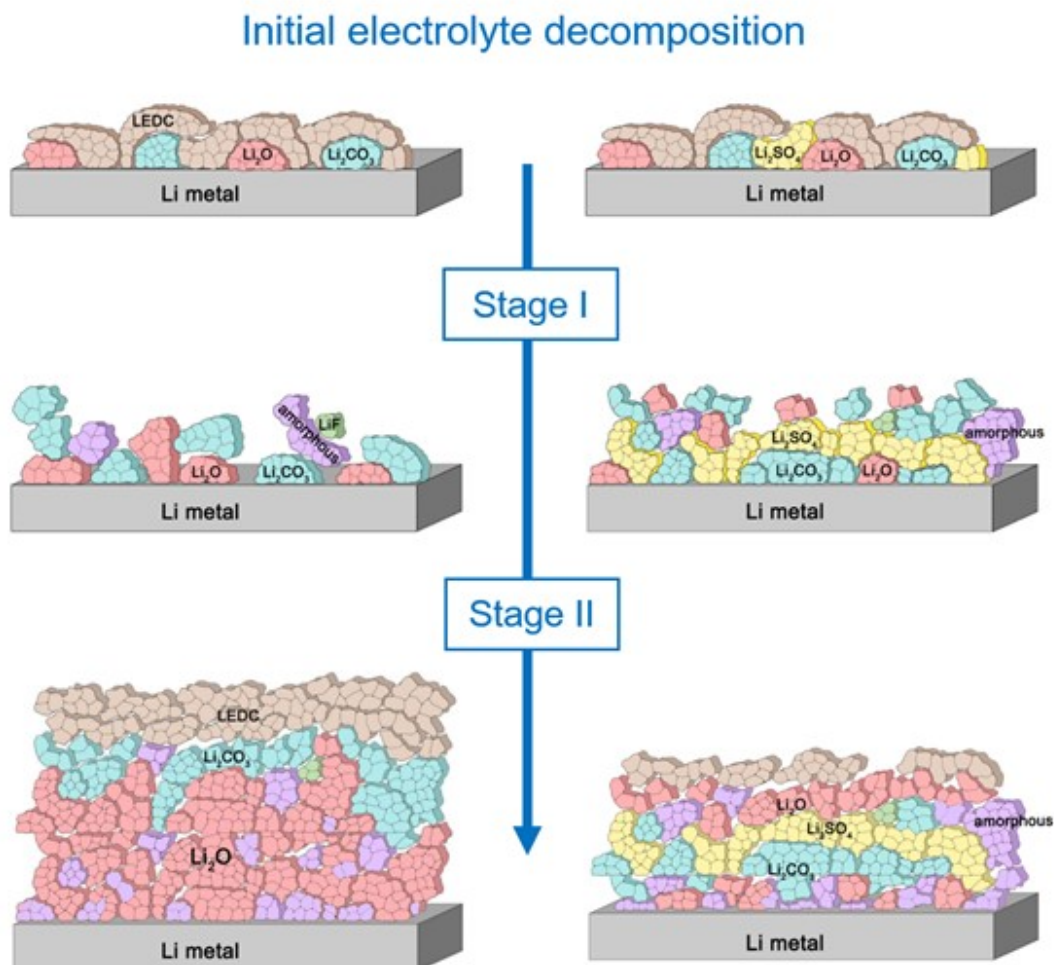


Fig. 6. a,b,c, Schematic of SEI formation on the Li_{Metal} electrode with blank electrolyte., due to the continuous decomposition of LEOC and Li_2CO_3 , lots of lithium oxide remains on the surface of the Li_{Metal} . The Li_2CO_3 decompose once touched Li_{Metal} surface. The partial exposure of the Li_{Metal} leads to the continuous reaction. **d,e,f,** SEI formation using the DTD electrolyte additive greatly expands the stability of SEI. DTD produces Li_2SO_4 , which cover lithium carbonate and inhibit the decomposition of lithium carbonate and electrolyte.

The SEI in the blank electrolyte is dynamically changing, which constantly consumes the cyclable lithium and electrolyte inventories (Fig. 6a to 6c). Calculations predict that the electrolyte molecules decompose to form lithium ethylene dicarbonate $\text{Li}_2\text{C}_4\text{H}_4\text{O}_6$ (LEDC), CO_2 , Li_2CO_3 , and Li_2O in the presence of excess Li atoms from Li_{Metal} during the initial stages of SEI formation¹⁸. The CO_2 gas increases the porosity of the as-formed SEI on Li_{Metal} and

reduces its passivation power. The Li_2CO_3 contacting Li_{Metal} produced the overlithiated phases, Li_2O and LiC_x , on the surface of Li_{Metal} . These reactions allow SEI layer to continuously increase in thickness, which reduces the cycle life of the battery.

In comparison, with sulfur-containing additives (PS and DTD), the resulting SEI became more stable and the consumption of electrolyte decreased (Fig. 6d to 6f). The addition of DTD produces Li_2SO_4 in addition to LEDC, Li_2O and Li_2CO_3 . The Li_2SO_4 and Li_2O can shield lithium carbonate and inhibit further decomposition of lithium carbonate on the top surface. While the Li_2SO_4 contacting Li_{Metal} produced the overlithiated products of crystalline Li_2O and amorphous Li_2S as a bottom buffer layer. As a result, the well-covered lithium carbonate in the middle of the SEI remains intact. The resulting SEI is thin and uniform due to the protective effect of Li_2SO_4 . In comparison, the amount of Li_2SO_4 produced by PS is less than DTD, as a result, its protective effect on lithium carbonate is not as strong. The SEI with PS and blank electrolyte has only partial coverage of Li_2CO_3 on the surface.

The first stage of the SEI formation reactions is the formation of the polyanion inorganic compounds as intermediates; while the second stage is the further decomposition of these polyanion compounds that are directly exposed to Li_{Metal} or electrolyte as shown by Figure 6. Overlithiated Li_2CO_3 leads to the formation of Li_2O and LiC_x when contacting with the Li metal. (This may also cause C, O, S impurities diffusion into the Li metal and thus the observed amorphous Li metal phase). LiC_x is electrically conductive, which diminishes the stability of the SEI due to electron channeling. In comparison, overlithiated Li_2SO_4 forms Li_2S and Li_2O , which are electronic insulators and prevent electron channeling, stabilizing the sandwiched Li_2CO_3 in the middle. Li_2SO_4 is a stable blanket on top of Li_2CO_3 as well to stop its reaction with electrolyte. Therefore, we believe the Li_2SO_4 is a more desirable component than Li_2CO_3 in the SEI. The Li_2CO_3 is very 'fragile' as found by our experiment and has to be wrapped by other phases for protection. Thus, desirable electrolyte additive should contain higher amount of sulfur. The SEI formed with DTD ($\text{C}_2\text{H}_4\text{O}_4\text{S}$) additive is better than PS ($\text{C}_3\text{H}_6\text{O}_3\text{S}$) additive due to more Li_2SO_4 and less Li_2CO_3 production, attributable to its higher sulfur content (the atomic percentage of sulfur in the DTD($\text{C}_2\text{H}_4\text{O}_4\text{S}$) and PS ($\text{C}_3\text{H}_6\text{O}_3\text{S}$) is 9% and 7.7%, respectively). Yet, the PS additive is still better than the blank EC-DEC electrolyte due to some content of sulfur that offers protection for the fragile Li_2CO_3 , which we have observed also but has dubious barrier properties. In addition, our experimental observation of Li_2CO_3 in the middle or outer layer of the SEI (but not directly contacting Li_{Metal}) suggests

that Li_2CO_3 further away from Li_{Metal} does not react with Li_{Metal} , likely due to slow electron transfer kinetics. Therefore, SEI formation is impacted by kinetic constraints during such reactions.

There are amorphous organic and amorphous inorganic components in the SEI. The amorphous organic polymeric phases are mechanically resilient upon Li metal stripping and plating³⁴. The amorphous inorganic components consist of both ceramic-like $\text{Inorg}_{\text{Amor}}$, and metallic Li_{Amor} . Similar percolating composite SEIs including inorganic phases of $\text{Li}_2\text{O}/\text{LiF}$ randomly distributing inside a polymer matrix are also observed in 1,3-dioxolane/1,2-dimethoxyethane based electrolyte, which ensures the stable cycling of Li-metal batteries. The optimal SEI should have Li_2O , LiF and overlithiated Li_2SO_4 to separate the Li_2CO_3 components from directly touching Li metal. The ionic conductivity of Li^+ in the nanocrystalline Li_2O , Li_2SO_4 , Li_2CO_3 and percolating amorphous phases that make up the SEI³⁵, plus interfacial diffusion along the grain boundaries and phase boundaries, should be further investigated. Reports showed that the space charge effect along the interfaces of these nanocrystalline inorganic phases can sometime generate a higher ionic carrier concentration and improves the ionic conductivity^{35, 36}. The success of the DTD additive is attributed to the formation of stable SEI with a gradient distribution of the organic and inorganic components that have high mechanical and chemical stability. In particular, a gradient amorphous matrix (polymeric→inorganic→metallic) with nanocrystalline embedded phases of Li_2SO_4 , Li_2CO_3 , Li_2O appear to be a general structural model.

Conclusions

To understand both the electronic insulation and percolating Li^+ transport across the SEI components, we first need to accurately determine the chemical phases and their nanoscale distribution in the SEI for different electrolyte formulations. Using aberration-corrected cryo-TEM, we captured atomic-scale pictures showing the composition and exact distribution of SEI components on the Li-metal anode. Surprisingly, HRTEM reveals that the Li_2O or the overlithiated amorphous phase (LiO_x , LiC_x , Li_xS) always buffer the Li_2CO_3 , and Li_2SO_4 from directly contacting the Li_{Metal} . The content of sulfur in the additive and resulting Li_2SO_4 crystals are desirable for a stable SEI on Li_{Metal} , which dictates the cyclability of the battery. Without additives, the naked Li_2CO_3 in the outer SEI layer is continuously reacting

with the electrolyte, resulting in bad cycling performance. However, the addition of sulfur-containing DTD additive produces large amounts of Li_2SO_4 , which and its overlithiated products (Li_2O and amorphous Li_xS and Li_xO) can securely sandwiched Li_2CO_3 from carbonate solvent decomposition in the middle. Our study reveals exactly why useful sulfur-containing additives work, and we have new directions for future better electrolyte design that specifically targets the controlling of the amorphous and crystalline components architecture in the SEI.

Author Manuscript

References:

1. Chen, Y. et al. Li metal deposition and stripping in a solid-state battery via Coble creep. *Nature* **578**, 251-255 (2020).
2. Goodenough, J.B. & Kim, Y. Challenges for Rechargeable Li Batteries. *Chem. Mater.* **22**, 587-603 (2010).
3. Xu, W. et al. Lithium metal anodes for rechargeable batteries. *Energy Environ. Sci.* **7**, 513-537 (2014).
4. Tikekar, M.D., Choudhury, S., Tu, Z. & Archer, L.A. Design principles for electrolytes and interfaces for stable lithium-metal batteries. *Nat. Energy* **1**, 16114 (2016).
5. Lin, D., Liu, Y. & Cui, Y. Reviving the lithium metal anode for high-energy batteries. *Nat. Nanotechnol.* **12**, 194-206 (2017).
6. Cheng, X.B., Zhang, R., Zhao, C.Z. & Zhang, Q. Toward Safe Lithium Metal Anode in Rechargeable Batteries: A Review. *Chem Rev* **117**, 10403-10473 (2017).
7. Bruce, P.G., Freunberger, S.A., Hardwick, L.J. & Tarascon, J.M. Li-O₂ and Li-S batteries with high energy storage. *Nat Mater* **11**, 19-29 (2011).
8. Armand, M. & Tarascon, J.M. Building better batteries. *Nature* **451**, 652-657 (2008).
9. Li, M., Lu, J., Chen, Z. & Amine, K. 30 Years of Lithium-Ion Batteries. *Adv. Mater.* **30**, 1800561 (2018).
10. Yang, C., Fu, K., Zhang, Y., Hitz, E. & Hu, L. Protected Lithium-Metal Anodes in Batteries: From Liquid to Solid. *Advanced materials* **29**, 1701169 (2017).
11. Aurbach, D. Review of selected electrode–solution interactions which determine the performance of Li and Li ion batteries. *Journal of Power Sources* **89**, 206-218 (2000).
12. Philippe, B. et al. Improved Performances of Nanosilicon Electrodes Using the Salt LiFSI: A Photoelectron Spectroscopy Study. *Journal of the American Chemical Society* **135**, 9829-9842 (2013).
13. Pinson, M.B. & Bazant, M.Z. Theory of SEI Formation in Rechargeable Batteries: Capacity Fade, Accelerated Aging and Lifetime Prediction. *Journal of the Electrochemical Society* **160**, A243-A250 (2012).

14. Younesi, R., Veith, G.M., Johansson, P., Edström, K. & Vegge, T. Lithium salts for advanced lithium batteries: Li-metal, Li-O₂, and Li-S. *Energy & Environmental Science* **8**, 1905-1922 (2015).
15. Aurbach, D., Daroux, M.L., Faguy, P.W. & Yeager, E. Identification of Surface Films Formed on Lithium in Propylene Carbonate Solutions. *Journal of The Electrochemical Society* **134**, 1611-1620 (1987).
16. Aurbach, D., Ein - Ely, Y. & Zaban, A. The Surface Chemistry of Lithium Electrodes in Alkyl Carbonate Solutions. *J. Electrochem. Soc.* **141**, L1-L3 (1994).
17. Liu, T. et al. In situ quantification of interphasial chemistry in Li-ion battery. *Nature Nanotechnology* **14**, 50-56 (2019).
18. Leung, K., Soto, F., Hankins, K., Balbuena, P.B. & Harrison, K.L. Stability of Solid Electrolyte Interphase Components on Lithium Metal and Reactive Anode Material Surfaces. *The Journal of Physical Chemistry C* **120**, 6302-6313 (2016).
19. Xu, K. Nonaqueous Liquid Electrolytes for Lithium-Based Rechargeable Batteries. *Chemical reviews* **104**, 4303-4418 (2004).
20. Smith, A.J., Burns, J.C., Zhao, X., Xiong, D. & Dahn, J.R. A High Precision Coulometry Study of the SEI Growth in Li/Graphite Cells. *Journal of The Electrochemical Society* **158**, A447 (2011).
21. Philippe, B. et al. Role of the LiPF₆ Salt for the Long-Term Stability of Silicon Electrodes in Li-Ion Batteries – A Photoelectron Spectroscopy Study. *Chem. Mater.* **25**, 394-404 (2013).
22. Philippe, B. et al. Nanosilicon Electrodes for Lithium-Ion Batteries: Interfacial Mechanisms Studied by Hard and Soft X-ray Photoelectron Spectroscopy. *Chem. Mater.* **24**, 1107-1115 (2012).
23. Zachman, M.J., Tu, Z., Choudhury, S., Archer, L.A. & Kourkoutis, L.F. Cryo-STEM mapping of solid-liquid interfaces and dendrites in lithium-metal batteries. *Nature* **560**, 345-349 (2018).
24. Wang, X. et al. New Insights on the Structure of Electrochemically Deposited Lithium Metal and Its Solid Electrolyte Interphases via Cryogenic TEM. *Nano Lett.* **17**, 7606-7612 (2017).

25. Li, Y. et al. Atomic structure of sensitive battery materials and interfaces revealed by cryo-electron microscopy. *Science* **358**, 506-510 (2017).
26. Peled, E. The Electrochemical Behavior of Alkali and Alkaline Earth Metals in Nonaqueous Battery Systems—The Solid Electrolyte Interphase Model. *J. Electrochem. Soc.* **126**, 2047-2051 (1979).
27. Peled, E., Golodnitsky, D. & Ardel, G. Advanced Model for Solid Electrolyte Interphase Electrodes in Liquid and Polymer Electrolytes. *J. Electrochem. Soc.* **144**, L208-L210 (1997).
28. Alvarado, J. et al. Bisalt ether electrolytes: a pathway towards lithium metal batteries with Ni-rich cathodes. *Energy & Environmental Science* **12**, 780-794 (2019).
29. Yang, Y. et al. Liquefied gas electrolytes for wide-temperature lithium metal batteries. *Energy & Environmental Science* **13**, 2209-2219 (2020).
30. Xu, Y. et al. Atomic to Nanoscale Origin of Vinylene Carbonate Enhanced Cycling Stability of Lithium Metal Anode Revealed by Cryo-Transmission Electron Microscopy. *Nano Lett.* **20**, 418-425 (2020).
31. Suo, L., Hu, Y.-S., Li, H., Armand, M. & Chen, L. A new class of Solvent-in-Salt electrolyte for high-energy rechargeable metallic lithium batteries. *Nat. Commun.* **4**, 1481 (2013).
32. Wang, X. et al. Glassy Li metal anode for high-performance rechargeable Li batteries. *Nat. Mater.* (2020).
33. Bi, Y. et al. Stability of Li_2CO_3 in cathode of lithium ion battery and its influence on electrochemical performance. *RSC Adv.* **6**, 19233-19237 (2016).
34. Wang, J. et al. Improving cyclability of Li metal batteries at elevated temperatures and its origin revealed by cryo-electron microscopy. *Nature Energy* **4**, 664-670 (2019).
35. Guo, R. & Gallant, B.M. Li_2O Solid Electrolyte Interphase: Probing Transport Properties at the Chemical Potential of Lithium. *Chem. Mater.* **32**, 5525-5533 (2020).
36. Zhang, Q. et al. Synergetic Effects of Inorganic Components in Solid Electrolyte Interphase on High Cycle Efficiency of Lithium Ion Batteries. *Nano Lett.* **16**, 2011-2016 (2016).

Acknowledgments:

This work was supported by Shenzhen Science and Technology Program (Grant No. KQTD20190929173815000), Guangdong Innovative and Entrepreneurial Research Team Program (Grant No. 2019ZT08C044, 2016ZT06N500), National Natural Science Foundation of China (22078144), Guangdong Provincial Key Laboratory of Energy Materials for Electric Power with project no. 2018B030322001, Shenzhen Peacock Plan (KQTD2016022620054656), Shenzhen DRC project [2018]1433, Key-Area Research and Development Program of Guangdong Province (2020B090919001), Shenzhen Clean Energy Research Institute (No. CERI-KY-2019-003). This work was performed at the Pico and Cryo-TEM Center at SUSTech Core Research Facility that receives support from Presidential fund and Development and Reform Commission of Shenzhen Municipality. JL acknowledges support by NSF CBET-2034902.

Author contributions: M.G., J. L., designed and supervised the experiment. B.H., Z.Z., Y. Z. carried out the cryo-TEM and battery testing; M.G., B.H., J. L., Z.Z. analyzed the data; M. G., J.L. wrote the manuscript; all authors discussed and contributed to the explanation and editing of the paper.

Competing interests

The authors declare no competing interests.

Sulfur-containing additives cause the SEI to preferentially generate overlithiated lithium sulfate and lithium oxide, which encapsulates lithium carbonate in the middle, limiting further SEI thickening and enhancing battery life by a factor of ten.

